Charge Exchange Recombination Spectroscopy at Wendelstein 7-X

O. P. Ford,[1, a)] L. Vanó,[1] A. Alonso,[2] J. Baldzuhn,[1] M. Beurskens,[1] C. Biedermann,[1] S.A. Bozhenkov,[1] G. Fuchert,[1] B. Geiger,[1] D. Hartmann,[3] R.J.E. Jaspers,[4] A. Kappatou,[3] A. Langenberg,[1] S. Lazerson,[1] R. McDermott,[3] P. McNeely,[3] T.W.C. Neelis,[4] N. Pablant,[1] E. Pasch,[1] N. Rust,[1] R. Schroeder,[1] E.R. Scott,[1] H.M. Smith,[1] Th. Wegner,[1] F. Kunkel,[1] R.C. Wolf,[1] and W7-X Team[1, b)]

[1)] *Max-Planck Institut für Plasmaphysik, 17491 Greifswald, Germany*
[2)] *CIEMAT, Avenida Complutense, 40, 28040 Madrid, Spain*
[3)] *Max-Planck Institut für Plasmaphysik, 85748 Garching, Germany*
[4)] *Eindhoven University of Technology, 5612 AZ Eindhoven, The Netherlands*

The Charge Exchange Recombination Spectroscopy (CXRS) diagnostic has become a routine diagnostic on almost all major high temperature fusion experimental devices. For the optimised stellarator W7-X, a highly flexible and extensive CXRS diagnostic has been built to provide high-resolution local measurements of several important plasma parameters using the recently commissioned neutral beam heating. This paper outlines the design specifics of the W7-X CXRS system and gives examples of the initial results obtained including typical ion temperature profiles for several common heating scenarios, toroidal flow and radial electric field derived from velocity measurements, beam attenuation via beam emission spectra and finally, normalised impurity density profiles under some typical plasma conditions.

I. Introduction

Wendelstein 7-X (W7-X) is an optimised stellarator built to demonstrate reduced neoclassical transport by optimisation of the magnetic field geometry[1–3]. For the detailed studies of the particle and energy transport required to assess the optimisation, accurate diagnosis of key plasma properties are necessary, particularly the electron and main ion temperature and density profiles T_e, n_e, T_i, n_i. A further critical ingredient is the radial electric field (E_r) that develops to equalise the electron and ion particle fluxes, which plays a central role in stellarator neoclassical particle transport[4].

From the beginning of the first phase of W7-X operation, the electron kinetic information has been well diagnosed by Thomson Scattering[5], Electron Cyclotron Emission[6] and a dispersion interferometer[7]. Line-averaged ion temperatures and radial electric field information was provided by an X-Ray Imaging Crystal Spectrometer (XICS)[4,8,9] based on low levels of argon injection. Ion density information was available only in the form of some preliminary Bremsstrahlung based effective charge Z_{eff} measurements[10].

In the latter half of the second experimental phase (OP1.2b), two 1.5MW positive-ion neutral beam injection (NBI) sources were commissioned[11]. This opened the possibility of making local measurements at high spatial and temporal resolution using active beam spectroscopy, comprised of Charge Exchange Recombination Spectroscopy (CXRS)[12–15] and Beam Emission Spectroscopy (BES)[16]. The improved ability to measure the temperature profiles comes as the NBI increases the importance of the ion heat transport channel compared to the first campaigns, where the electron-channel dominated in Electron Cyclotron Resonant Heated (ECRH) plasmas[17].

As well as improved ion temperature and radial electric field measurements, the active beam spectroscopy provides the only measurements of the neutral beam density n_b, toroidal plasma flow v_ϕ and profiles of the intrinsic fully-stripped low-Z impurity densities (n_Z) in the plasma core. As well as the indirect measurement of the effective charge (Z_{eff}) via the concentration of all prevalent impurities, CXRS may be able to directly measure hydrogen (main ion) density (n_i) from the H_α spectrum.

II. Diagnostic Hardware

In order to provide robust and reliable measurements of these essential quantities at high resolution, much of the W7-X CXRS was broadly based on the CXRS system of the ASDEX-Upgrade tokamak[15,18] which has similar plasma minor radius, temperatures and densities and almost identical NBI sources. Significant differences are the larger carbon and oxygen impurity concentrations in W7-X due to the large surface area of carbon first-wall and divertor and the higher Bremsstrahlung background level due to plasma densities up to $2 \times 10^{20}\text{m}^{-3}$. The major differences in the final design are in the front-end optics, where a 'plug-in' immersion-tube is typically used at W7-X due to limited space in-vessel and the presence of the cryostat for the super-conducting magnets, in contrast to the in-vessel mounted components at ASDEX Upgrade.

The CXRS/BES system is split into three parts: 1) The front-end optical components, 2) a set of 172 90m long fibres that transfer the collected light to a laboratory outside the torus hall and 3) the spectrometers, data acquisition and control equipment in the laboratory. All components use the same $400\mu\text{m}, 0.22\text{NA}$ fibres and are terminated with standard FC/PC connections to allow complete flexibility of configuration between and during measurement campaigns.

[a)] Corresponding author. E-Mail: rsi19(at)oliford.co.uk
[b)] For the complete member list, please refer to T. Klinger et al., Nuclear Fusion 59, 112004 (2019)

A. Observation positions and radial resolution

The front-end optics consist of two dedicated immersion tubes, one viewing toroidally and one at 45° to the toroidal for the purpose of detecting poloidal flow. These are named according to their port location: **A** for the toroidal view and **M** for the 45° view. An additional low-resolution optic **T** is built into an immersion tube shared with the NBI heat-shield thermography diagnostic. The full W7-X diagnostic port names are AEA21, AEM21 and AET21 respectively, designating diagnostic-ports in the half-module 2.1.

Each optical system images one or more rows of points along the NBI path onto a set of fibres by means of a mirror and two lenses. The optical collection volume for each fibre approximates to a 2cm diameter cylindrical 'line of sight' (LOS) that passes through one or both beams. Figure 1 shows a 3D view of the lines of sight and the two NBI paths, along with their projections onto a top-down view of the plasma.

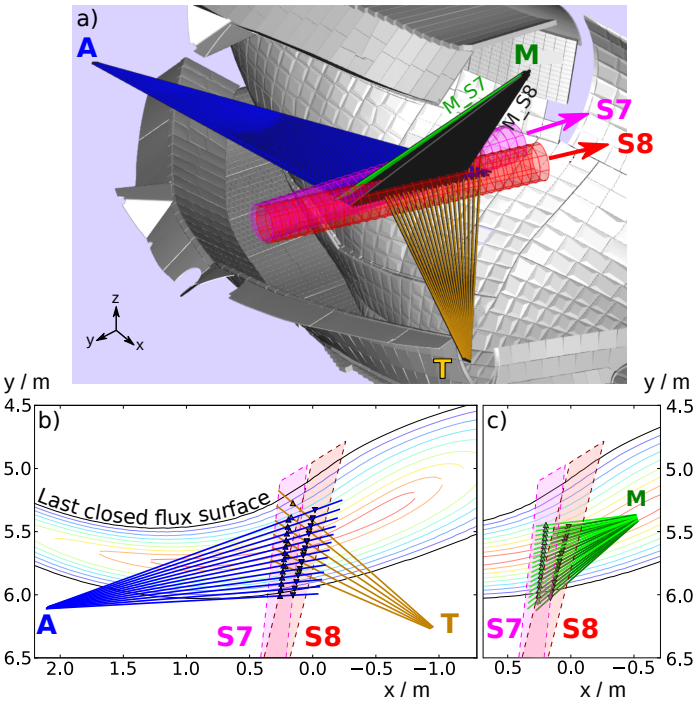

FIG. 1. Lines of sight of the three CXRS observation systems. a) 3D view of the inner wall and lower divertor of half module 2.1 with the two NBI sources 'S7' (magenta) and 'S8' (red) as well as lines of sight of the three CXRS optical systems: **A** (blue), **M** (green) and **T** (orange). b,c) Horizontal cut of plasma at beam height and projection of CXRS lines of sight.

Since the **M** system views the two horizontally separated beams from above, two rows of lines of sight are needed to target the highest intensity part of each beam respectively. A simplified effective observation position is calculated as the beam-intensity weighted average position along the line of sight. For the **M** and **T** systems, this varies strongly with which beam is active. Figure 2 shows the effective observation positions in the poloidal plane for each system and for the **M** system with each beam source. The two primary systems (**A** and **M**) have two additional perpendicular sets of fibres (labelled -X1 and -X2) to allow for measurements of the NBI beam width and divergence from the beam emission spectra. Three of the points on A21-X2 also allow for measurements at the very core of the plasma, which does not sit along the NBI beam axis.

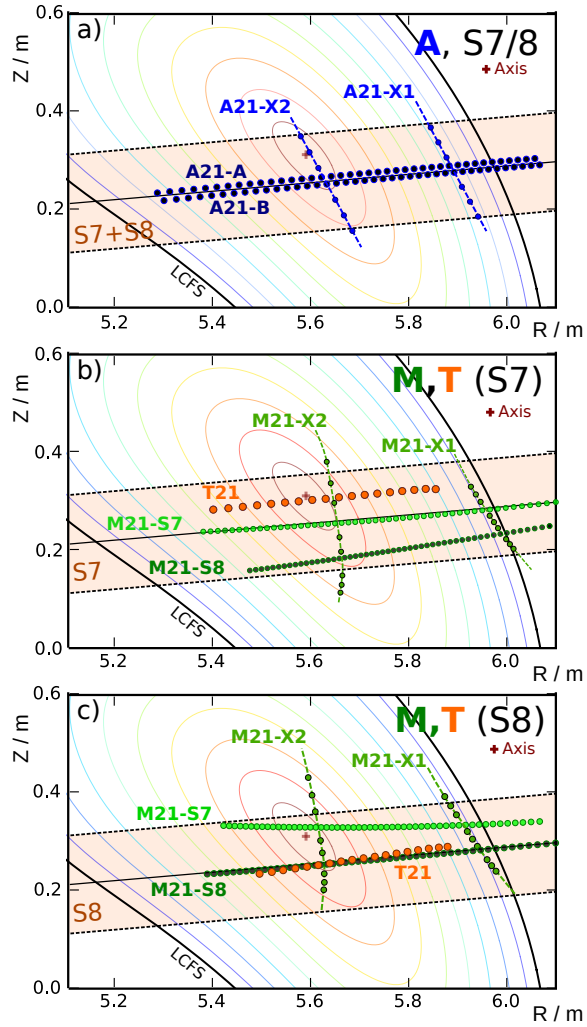

FIG. 2. CXRS effective measurement positions in the poloidal plane in relation to flux surfaces of the standard vacuum magnetic configuration. a) The toroidal **A** CXRS system including two rows of fibres 'A21-A' and 'A21-B' and two perpendicular arrays 'A21-X1' and 'A21-X2'. The positions are equivalent for either NBI source. b) 45° systems **M** and **T** when viewing NBI source 7 and c) when viewing NBI source 8. The **M** systems have two rows 'M21-S7' and 'M21-S8' targetted at each beam axis respectively and two perpendicular arrays 'M21-X1' and 'M21-X2'. The **T** system has only a single array of 20 fibres.

From figure 1, it can be seen that the toroidal **A** system views the beam with lines of sight almost parallel to the flux surfaces across the width of both beams, lead-

ing to a well localised measurement in normalised radius. The other two systems have poorer resolution, particularly towards the plasma core. Figure 3 shows the radial resolution of the outboard points in effective plasma radius for each of the systems. This is calculated from the intensity weighted variance of the effective radius along the line of sight, assuming a Gaussian beam density with 20cm FWHM in the W7-X standard vacuum magnetic configuration. Due to the different beam geometries, the resolution depends on the active beam source and the highest resolution is achieved with the use of beam S7. Use of both beams simultaneously (not shown in figure 3) gives a resolution for the **A** system similar to that for source S8 alone. For the **M** system, both beams lead to a significantly poorer resolution of up to 12cm in the core. The inboard lines of sight are not shown in figure 3. For system **A**, they have almost the same resolution as the outboard points. Systems **M** and **T** have a considerably lower inboard resolution of more than 12cm.

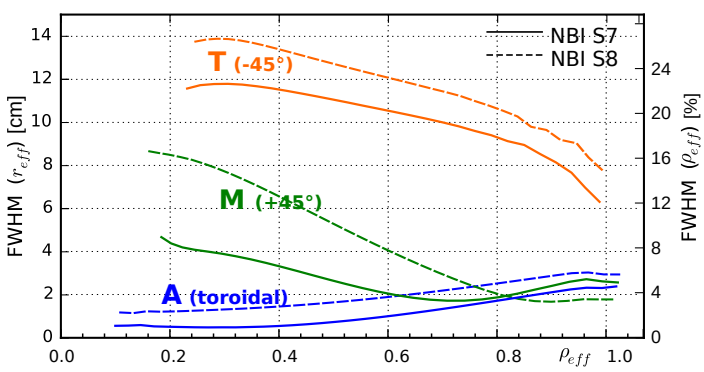

FIG. 3. CXRS effective radial resolution for the out-board lines of sight: Full-width half-maximum in effective radius (r_{eff}) of beam intensity distribution along each line of sight, versus average normalised radius ρ_{eff} under operation of individual beam sources 7 and 8.

B. Observation hardware

The **A** and **M** optical systems consist of a 2m immersion tube with standard welded CF-Flange window at the inside end. At the planned peak performance of W7-X, heat loads of up to $100kWm^{-2}$ are expected on the plasma facing components from plasma radiation and ECRH stray radiation. Combined with the planned long pulse operation of up to 30 minutes, this places extreme design requirements on W7-X diagnostics, which are covered in detail elsewhere[19]. However, since the CXRS system requires the NBI, which is only available for periods of up to 10s every few minutes, the sensitive components can be covered for longer periods, significantly reducing the design requirements on them. The welded CF-Flange windows are recessed from the plasma edge and view directly onto an aluminium mirror, as shown in figure 4 for the **A** system. In this case, a 120 x 60mm rectangular mirror is used. The **M** system has a conceptually equivalent design, although uses a 120mm diameter circular mirror due to the differences in surrounding port structure. In both cases, the mirrors are encased in a stainless steel shutter that will remain closed except during the short periods of NBI operation, protecting the mirrors and windows from heat loads and deposition or erosion during long pulse operation. The mirrors are precision machined from a special aluminium alloy RSA-905 for a high stiffness and high maximum temperature of 350^oC. In later campaigns, the stainless steel mirror frame will need to be actively cooled to keep it below this temperature during long-pulse operation.

Inside the immersion tube a carriage is inserted, which carries two plano-convex lenses and the fibre bundle head, also depicted in figure 4. Unfortunately, the use of commercial compound objectives are precluded by the strict material requirements for W7-X. These requirements arise due to the desire to minimise ferromagnetic materials that can cumulatively introduce significant field errors, to which the stellarator confinement is particularly sensitive and also to reduce the nuclear activation during the planned long-pulse deuterium operation. The disadvantage to this is a curved and significantly distorted image focal surface.

The fibre head was designed by ray-tracing the set of desired focal points evenly distributed along the beam axis to the fibre focal surface. A compromise between the regular distribution of focal points along the beam axis, optimal focus across the full visible wavelength range and feasibility of manufacturing of the fibre head was made and the final locations used to construct the fibre head. The final locations were also used to ray-trace the numerical aperture of the fibre back towards the beam to produce the lines of sight discussed in the previous section and check that the final focal spot sizes are smaller than the geometric resolution shown in figure 3.

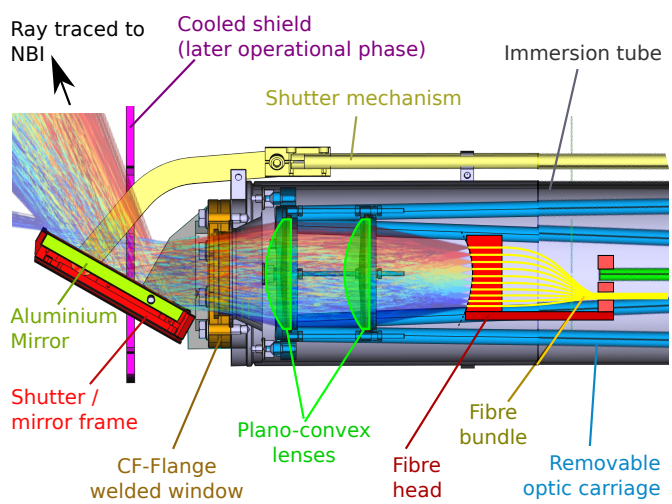

FIG. 4. CXRS optical observation hardware at the vacuum barrier of the toroidal **A** port system, including ray-tracing of several optical fibres.

C. Spectrometers

The primary measurements of the CXRS are made by a three colour channel high-étendue spectrometer[20] which was originally designed as a prototype for ITER and previously used on the TEXTOR[21] and ASDEX-Upgrade[22] tokamaks. The spectrometer, known as the 'ITER-Like spectrometer' (ILS) has 54 fibres, each of which are split into three colour channels to ultimately provide all the primary measurements at the same 54 spatial locations. A 'red' channel covering the range $648 - 666nm$ resolves the beam emission and charge exchange spectrum of the H_α line. A 'green' channel over the range $518 - 534nm$ covers both the strongest visible carbon charge exchange line C^{VI} at $529.07nm$ and a strong neon line Ne_X at $524.9nm$. Finally, a 'blue' channel covers the range $461nm - 474nm$ which resolves the He_{II} line at $468.52nm$. Two of the ILS input fibres are reserved for calibration while the remaining are distributed across the full radial profiles of the **A** and **M** optical systems in order to provide complete coverage of the most important measurements (T_i, E_r). These are interlaced on the spectrometer in order to mitigate the effect of any systematic error in the wavelength calibration across the CCD on the difference between toroidal and poloidal flows at the same location. This is done to maximise the sensitivity of the flow measurement decomposition.

To examine impurities not covered by the ILS, two variable wavelength spectrometers were assembled from a ruled diffraction grating, two photographic objective lenses, a high performance 1024 x 1024 pixel CCD camera and common commercially available high-quality optical components. Figure 5 gives the salient details. The optical setup was based on the main ASDEX-Upgrade CXRS spectrometers[15] with the primary difference being the use of a larger CCD chip, increasing the number of imaged fibres by a factor of two to 45 in total, at the expense of a factor of two in maximum frame rate. The extra fibres suffer a significant, but tolerable vignetting of at worst $\sim 60\%$. The focus quality is sufficient to achieve less than 1% cross-talk between fibre channels despite tight packing of the fibres and a wavelength resolution of 42pm at the minimum slit width of 15μm up to 1nm when imaging the full 400μm fibres.

III. Calibration

A. Wavelength, dispersion and instrument function

Calibration of the wavelength offset, dispersion and instrument function is performed using neon or xenon pencil lamps. During installation, all fibres are lit, providing multiple spectral lines on all channels. These are fitted with a modified Gaussian with free exponent, known as a super-Gaussian function ($\sim \exp(-|x/\sigma|^\alpha)$). This line shape fits well to all lines and channels of all spectrometers and allows for the more top-hat like instrument function obtained when a wide slit is used to achieve higher signal to noise. No assymetry was observed in the instrument functions.

The dispersion and instrument function are very robust on all of the spectrometers and variations are small enough to have no discernible effect on the derived ion temperatures. The absolute wavelength can however vary significantly which affects the derived flow measurements and radial electric field. To assess this during operation, two fibres on each spectrometer are left unconnected and are periodically lit with the calibration lamp to correct for small slow drifts in the wavelength offset over time. The variable wavelength spectrometers were calibrated with the two fibres before and after every movement of the grating position, and before and after important operational days. In future, the automatic illumination of the calibration fibres will be performed before and after every discharge. Nevertheless, it will still need to be assumed that returning the grating to a given position maintains all but the wavelength offset relative to the full chip calibration performed pre- or post-campaign.

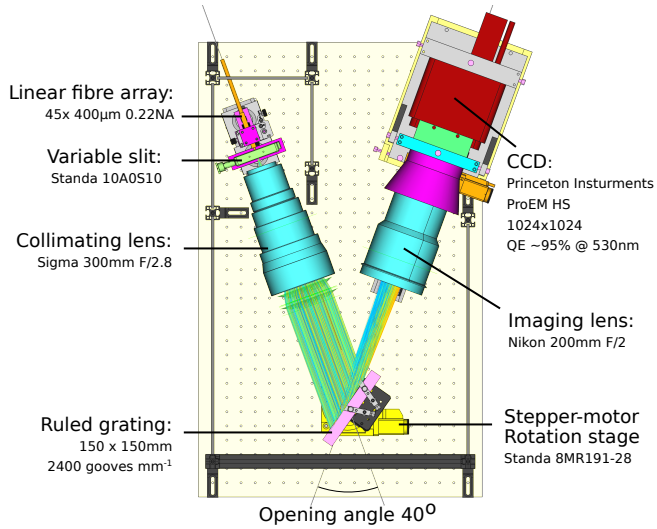

FIG. 5. Variable wavelength spectrometer design

B. Alignment

The position and focus is initially set in the laboratory by back lighting the optical fibres and projecting the focal spots onto a plane at the distance of the neutral beam. The designed target positions on the plane are calculated using a ray-tracer and the optics adjusted to matched these calculated coordinates. Once the optical carriage is installed in the immersion tube, the optical fibre head position can be fine-adjusted relative to the lenses from outside the machine if necessary. For the **M** and **T** ports this is done while observing the back-lit positions on the vessel wall from inside the vessel and matching these to the wall intersection position calculated by the ray-tracer. This is not possible for the A-port as access to module 2, where the NBI is situated is no longer possible once the A-port is in place. Instead, the toroidal viewing video camera system in port 'Q21' (nearby the toroidal A-port shown in figure 1) is used im-

mediately prior to the campaign. From an image of the vessel structure, points are identified in the image and a 2D mapping of machine coordinates to camera pixel coordinates is found. Several fibres are back-lit and the projected wall-intersection spots in the camera image are compared with those calculated by the ray-tracer, transformed to a 2D image position via the mapping. If a significant deviation is found, the fibre head position can be adjusted from outside the vessel and the measurement repeated. Otherwise, the measured positions are used to calculate the lines of sight used in the data analysis. Figure 6 shows the camera calibration image and final position mapping for the A-port system after adjustment, which leads to observation points at most 10mm from the original design locations.

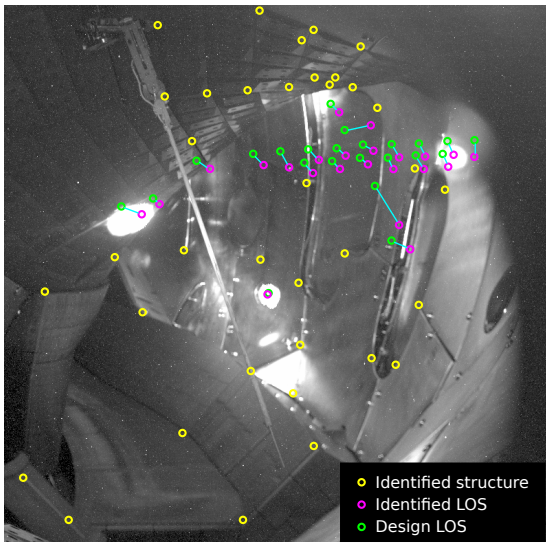

FIG. 6. Video camera image of wall structures including points identified on image and in CAD data to determine transform of image to 3D coordinates (yellow). Also shown are wall intersection spots of back-lit CXRS fibres calculated from as-designed alignment (green) and measured from image (magenta).

C. Intensity

In order to derive absolute impurity densities, an absolute calibration of the complete optical system, from first mirror through to the CCD is required. The desired default fibre connection is set before the vacuum vessel is closed at the start of the campaign and the whole system illuminated with a comercial absolutely calibrated integrating sphere. For the **M** and **T** systems this is done in-vessel. For the **A** port, the optics are installed into the immersion tube, the fibres connected and the complete calibration performed outside the machine immediately before installation of the port. Sufficiently flexibility is designed into the CXRS fibres to allow the installation of the port with the complete CXRS system without disconnecting the fibres and hence disturbing the calibration.

IV. Data analysis

For the impurity charge exchange, a simple Gaussian fit is conducted and intensity, position and width used to calculate the impurity density, velocity and temperature respectively. The temperature is corrected for the instrument function broadening using correction factors calculated from the super-Gaussian functions determined from the pencil lamp calibration data. For a range of temperatures, a Gaussian representing the thermal Doppler broadening is convolved with the instrument function of each channel and the result is fitted with a Gaussian to determine the apparent temperature. Above 50eV, the result is well described as a conventional Gaussian due to the dominance of the Dopper width. The calculated relation of true to apparent temperature is used in reverse to correct the fits to the measured spectra. A similar proceedure is used to correct for the broadening by fine-structure and Zeeman splitting, as described elsewhere[23]. Corrections due to the velocity dependence of the charge exchange cross-section have not been included, as these are expected to be insignificant ($< 20eV$) at the ion temperatures observed in W7-X[24].

The correct handling of the passive edge emission collected by all lines of sight as they pass through the plasma edge is critical to interpretation of the spectra. For short 'blips' or fast modulation of the NBI, it is possible to linear interpolate the spectrum before and after the NBI is active over time and subtract this from the data of each frame. However, for longer injection, a dual-Gaussian free fit is necessary. For core lines of sight where the active component has relatively large width due to the high temperature, the fit is well determined. Figure 7a shows the spectrum of a core spatial channel and figure 7b shows the time evolution of derived active and passive intensities. It can be seen that the passive emission contributes almost half of the observed intensity and changes rapidly after the switch on of the beam, increasing by 30% in $\sim$ 30ms. This is believed to be due to neutrals released either from the beam duct or beam dump during NBI operation. It is clear that after $\sim 30ms$, the simple linear interpolation of the background is no longer valid. Figure 7c shows the temperature profiles derived using the two methods at $t = 5.0s$. In both cases, 100ms of data have been averaged, making the statistical error insignificant and so no error bars are plotted. The remaining scatter is entirely due to systematic errors, most likely due to the misinterpretation of the passive emission. The linear interpolation (yellow points) clearly shows negatively biased outliers resulting from underestimation of the passive contribution on those channels. The outliers are eliminated in the dual-Gaussian fit results (blue points). However, near the plasma edge $\rho_{\text{eff}} > 0.7$, the passive and active components have similar spectral widths making the dual-Gaussian fit highly ambiguous and leading to overestimated T_i compared to the linear interpolated approach which agress slightly better with the T_e profile from the Thomson Scatting diagnostic, as is expected physically in this region. The problem of passive emis-

sion is exacerbated in stellarators by the strong damping of the toroidal flow which otherwise (e.g. in tokamaks) gives a significant line shift of the active component relative to the passive. The addition of equivalent lines of sight that do not view the beam, e.g. in a different module, could help to identify the temporal evolution of the passive emission. However, this would not be of use if the increased passive emission is caused by neutrals released from the beam duct or beam dump.

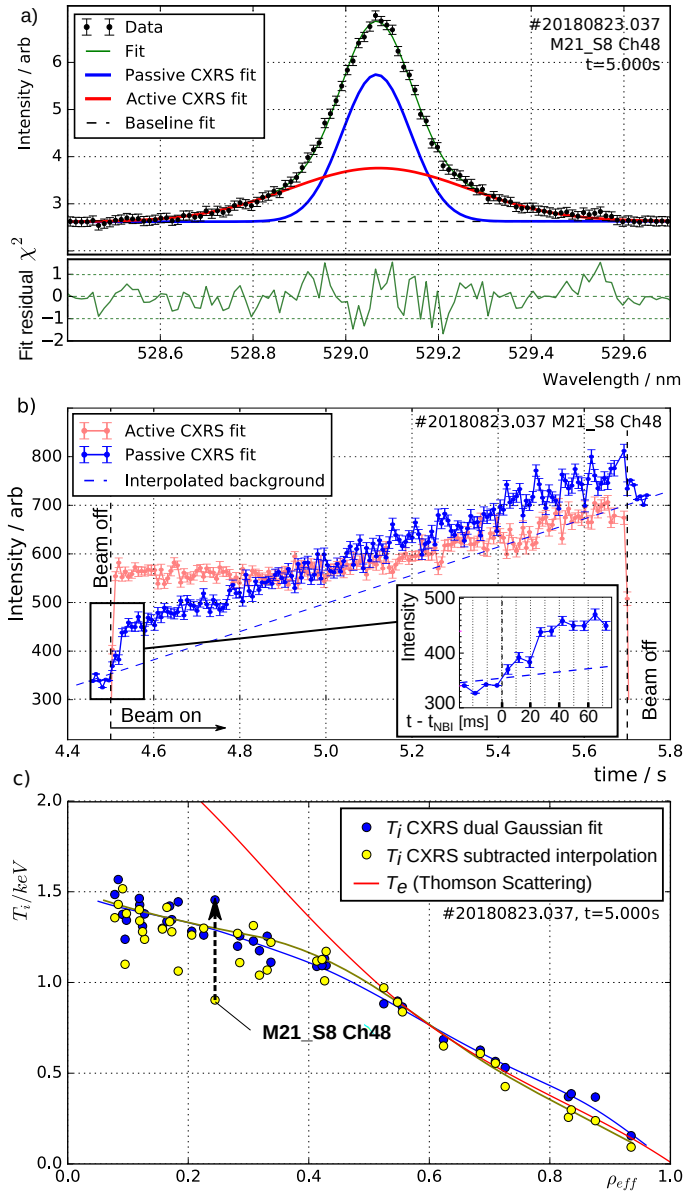

FIG. 7. a) Typical spectrum, fit and residual for a core channel during continuous NBI. b) Time dependence of fitted intensity of the active component and of the passive component compared to a linear interpolation of the pre- and post-beam passive intensities. The sub-frame shows the first 60ms after NBI swtich-on magnified. c) Ion temperature profiles derived from the dual Gaussian fit and from interpolated background subtraction. The black arrow highlights the channel shown in (a) and (b) and highlights the improvement obtained by dual Gaussian fit method.

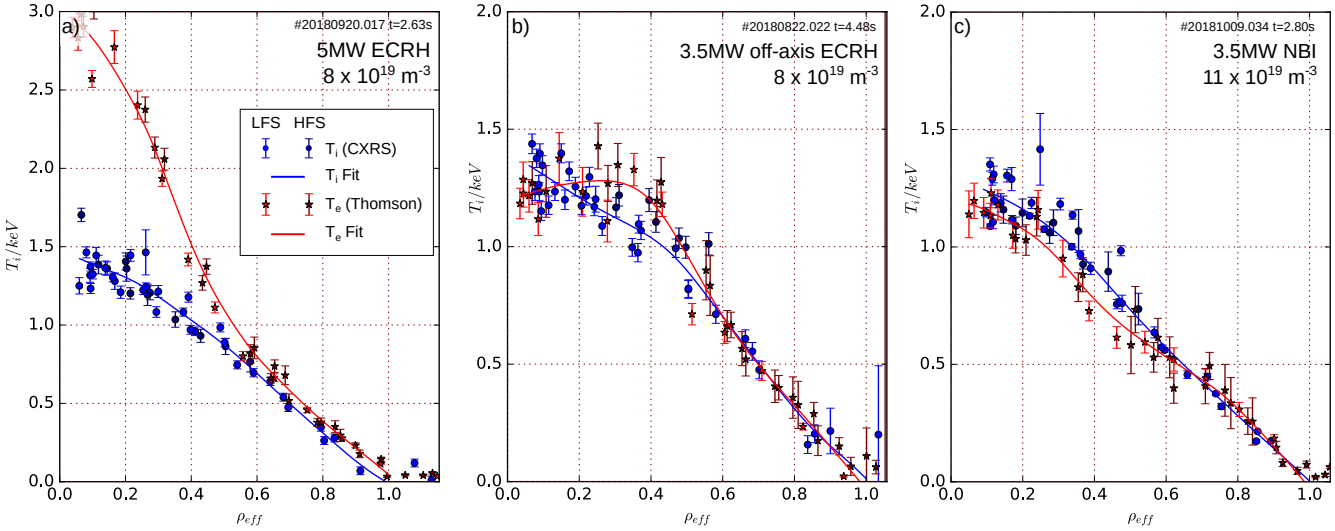

FIG. 8. Ion (blue) and electron (red) temperature profiles from CXRS and Thomson Scattering respectively, for typical W7-X plasmas under different heating conditions: a) On-axis and b) Off-axis ECRH heating and c) NBI heating. High-/low- field side (HFS/LFS) points are shown in darker/lighter colours respectively.

A. Ion temperature profiles

Figure 8 shows the ion temperatures derived from C^{VI} at 529nm with the ILS spectrometer for three typical heating scenarios at W7-X. Also shown for comparison is the electron temperature profiles of the Thomson Scattering system[5,25]. The figure gives a good representation of the profile quality achieved by the main CXRS system for most NBI shots in the OP1.2b campaign including both integration over $20ms$ beam blips shown in figures 8a and b and $7.5ms$ integration during continuous beam operation in 8c. The latter represents one of the worse case scenarios, where high electron density leads to an intense Bremsstrahlung background and strong beam attenuation, while continuous NBI necessitates dual-Gaussian fitting. Despite this, the data quality remains very good, even at the plasma core. The strong core ECRH heating and moderate density in figure 8a leads to poor electron-ion heat coupling in the core such that only near the edge is $T_e \approx T_i$. Off-axis ECRH and higher n_e in figure 8b gives much stronger coupling and $T_e > T_i$ only directly under the ECRH heating peak at $r_{\text{eff}} \approx 0.3$. Finally, pure-NBI heating in figure 8c shows that the NBI's preferential ion heating leads to a higher T_i over nearly the whole radius. The spatially broad heating profile of the NBI, similar power and slightly higher electron density leads to very similar profiles to the off-axis ECRH case. The absolute values, profile shapes and positions appaear consistent with the Thomson Scattering electron temperature profiles and suggests that no signficant issues with the spatial alignment, instrument function and dispersion calibrations are present.

B. Velocities and radial electric field

Figure 9a and b shows the velocities along the lines of sight measured by the CXRS system during a 20ms beam blip into a typical ECRH heated plasma. These are corrected for the apparent shift in central wavelength due to the velocity dependence of the charge exchange cross-section[24] and finite-lifetime effects[26]. Fine-structure and Zeeman corrections are currently not included and are expected[23] to introduce a constant offset of about 5 km/s.

By assuming incompressible flow, it is possible to calculate the local parallel and perpendicular flows at any point in the stellarator from profiles of the radial electric field $E_r(\rho)$ and net toroidal flow $v_{\|}(\rho)$[27,28]. Figure 9 shows the E_r (c) and $v_{\|}$ (d) determined by fitting to the measurements in sub-plots (a) and (b). The fit also included a single constant offset as a free parameter, which is required to find a consistent solution for the flows observed. The data from the otherwise secondary **T** port provides a strong constraint in this case, since it views the perpendicular flow with the opposite sign to the **M** system. This constant offset also largely elimintes the offset due to the fine struture and Zeeman effects. It is usually determined to be around $+5km/s$ (red shift) although varies over the course of each day. The calibration of the ILS green channel was checked after the campaign and found to drift after power-on of the camera, exponentially approaching an offset of $\Delta\lambda = 11pm$ ($\Delta v = 6.2km/s$) with time scale length of 80 minutes. Since this drift is clearly far larger than the statistical noise, the pencil lamp calibration will be performed automatically between shots in future campaigns. It should be noted that the analysis outlined here also ignores line-integration effects over the width of the NBI beam which may significant for the **T** and **M** port lines near the magnetic axis. A detailed account of the flow calculation and all of the corrections will be the subject of a subsequent publication.

Also shown in figure 9c and d are the neoclassical calcu-

lations of ambipolar radial electric field and C^{6+} net parallel velocity conducted with the DKES code[29,30], based on experimental profiles for H ions and electrons. A radially constant $Z_{\text{eff}} = 1.5$ is assumed and the shaded band shows the range of these calculations for ± 0.3 variation of Z_{eff}. The inferred E_r profile is similar in form to the predictions, revealing a small region of electron-root conditions ($E_r > 0$) that transitions to ion root at $\rho_{\text{eff}} \sim 0.3$. However, the strength of the ion root radial field at $\rho \sim 0.7$ appears much stronger than expected. This will later be cross-checked with measurements from Doppler reflectometry and XICS. The toroidal flow measurements indicate a small positive flow in the plasma core, which is not expected from neoclassical predictions. As this is of the same order as both the velocity corrections and the spectrometer drift, it will require careful examination, for instance by cross-checking with the flows measured by the variable wavelength spectrometers. Additionally, the model is unable to fit the HFS points of the toroidal view which may indicate some influence of the subtracted passive background as detailed in section IV, since these channels have a relatively strong passive contribution.

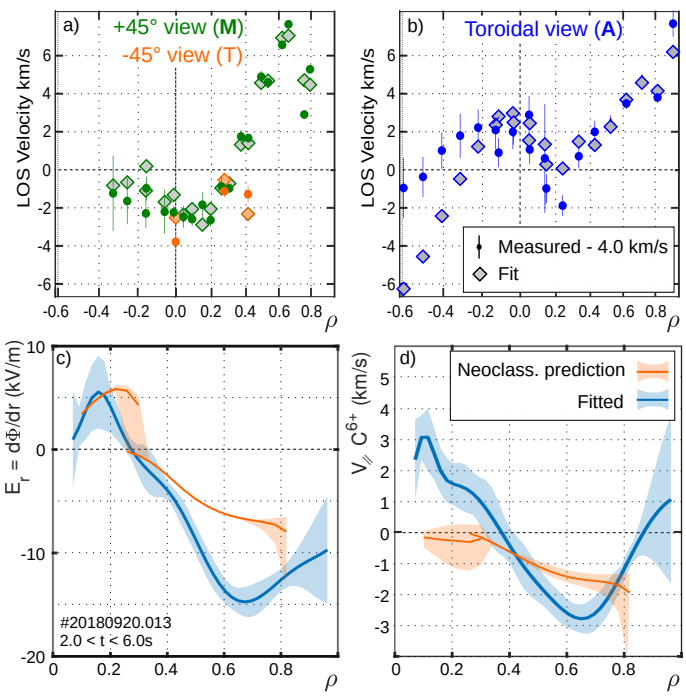

FIG. 9. Corrected line of sight parallel velocities measured from the $C^{VI}529.1nm$ line on a) the $\pm 45^o$ (**M**, **T**) and b) the toroidal (**A**) observation systems. $\rho_{\text{eff}} < 0$ indicates high-field (inboard) side measurements. c) Radial electric field and d) net toroidal rotation profiles inferred by a fit to the line of sight velocities in (a/b). The predictions from this fit are shown in (a/b) as grey diamonds. Also shown in (c/d) are the predicted neoclassical radial field and toroidal flow calculated by the DKES code, with uncertainty due to $Z_{\text{eff}} \pm 0.3$.

C. Beam emission

The hydrogen Balmer alpha (H_α) spectrum measured by the ILS contains a multitude of useful information. As well as the possibility of direct measurement of the hydrogen density and temperature[31], the spectrum contains the collisionally excited emission of beam neutrals, revealing information about the beam neutral density. This is vital for validating beam models which will provide the beam fast-ion birth profile and hence the NBI heat and particle source profiles needed for accurate transport analysis in NBI heated plasmas. In the simplest case, the beam attenuation provides a direct accurate measurement of the beam shine-through, vital for power balance calculations. Additionally, the local beam neutral density is needed for proper interpretation of the impurity charge exchange intensities.

Unfortunately, the H_α spectrum is a complex mix of several components and must be forward modelled carefully. Figure 10a shows the H_α spectrum for a single line of sight measured by the red channel of the ILS. 17 Gaussians are fitted to the measured data in order to account for the three stark-split components of each of the 3 beam energy components, the cold passive H_α emission from the plasma edge, the thermal active charge exchange emission and several impurity lines from the edge. The amplitude, width and positions of all Gaussians are free parameters but the positions of all 9 beam energy components are restricted to nearby their Doppler shift calculated from the angle between line of sight and the beam. In cases such as that shown, the fit is unambiguous and the density of all 3 beam energy components can be easily determined. In cases where the angle between beam and line of sight is more perpendicular, some or all of the energy components coincide with the thermal/halo charge exchange and the C^{II} radiation seen at $658nm$ in figure 10. In such cases, or where both beam sources are active, the fit cannot be easily resolved. A complete consistent forward model of the beam is expected to alleviate the problem to some degree and will be covered in a later publication. For this simple case the first two energy components are relatively robust and the derived normalised beam densities from the **A** system can be seen in figure 10b. Also shown is a simple prediction based on the electron density profile measured by the Thomson Scattering system and beam-stopping coefficients from ADAS[32]. The overall decay rate and it's dependency on plasma density is well reproduced although structures can be seen in the measurements that are most likely artifacts of the fitting ambiguity. The beam stopping coefficients used assume a pure hydrogen plasma but the impurity contribution is not expected to be large in these ECRH plasmas, where Z_{eff} measurements are typically around 1.3 and the most significant impurity species is carbon, for which the beam stopping coefficients are of the same order as those of hydrogen."

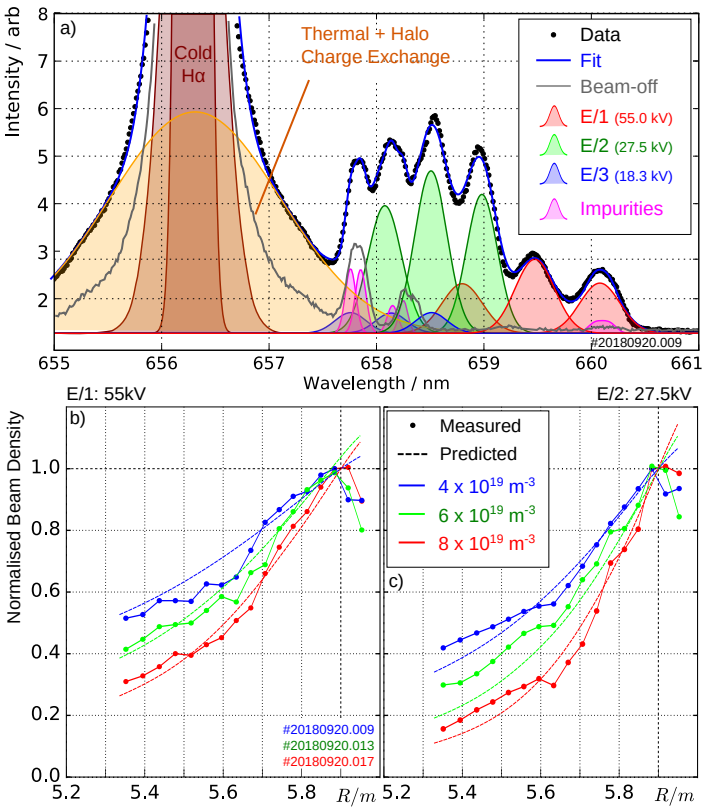

FIG. 10. a) Hydrogen Balmer-alpha spectrum measured by the ILS for a single line of sight on the **A** (toroidal) system. b) Derived normalised beam neutral density of the first two energy components at three different nominal plasma densities, compared with predicted attenuation based on electron density measurements.

D. Impurity densities

Calculation of impurity densities from charge exchange intensity is typically performed using an absolute intensity calibration of the diagnostic and a validated model of the neutral beam attenuation to provide the absolute donor neutral densities at each energy. Alternatively, an approximation for the quantity n_Z/n_e can be derived from the ratio of the charge exchange line intensity to beam emission intensity at the same location[33]. From this quantity, the impurity concentration $n_Z/\sum_i n_i$ can be calculated if only a single impurity species is dominant in the plasma. The ILS spectrometer has been designed with this in mind, measuring both CX and BES signals on the same lines of sight[21]. Nonetheless, calculation of the absolute concentration must still take into account all energy components, the relative sensitivity of the spectrometer channels, the effective charge exchange and beam emission coefficients and their dependence on the local plasma parameters. Also, at higher densities, a significant contribution to charge exchange also originates from the $n = 2$ states of the beam halo[34], which necessitates an accurate model of the halo as this is not accounted for by the relative intensity ratio method.

A thorough analysis of the impurity concentration profiles and transport during the last W7-X campaign is underway[35] and will use both this relative CX/BES intensity method as well as the modelled absolute beam and halo densities[34] to derive accurate absolute impurity profiles of the low-Z impurities present in W7-X including carbon, oxygen and boron that was introduced for wall conditioning[36].

In the meantime, the gross features of the normalised profile shape can be determined directly from I_{CX}/I_{BES}, since the various factors mentioned above are not expected to vary significantly over the plasma radius. Figure 11 (green) shows the normalised carbon concentration profiles at the start (a) and end (b) of a pure NBI phase, revealing strong peaking of the carbon concentration in the plasma core during pure NBI operation. Given the high electron densities reached at the end of such pure NBI phases, the halo could contribute up to 50% of the signal in the core[34]. However, even at this level, it could only account for a small amount of the observed intensity peaking. The observation of this peaking, which has long been anticipated in W7-X[37], demonstrates that the application of the CXRS diagnostic at this machine will be a critical tool in the investigation of stellarator specfic impurity physics.

The CXRS system was also used to observe dynamic events such as boron and iron injection from the W7-X laser blow-off (LBO) injection system[39], boron pellets from the boron pellet dropper[40] and iron and carbon injection with TESPEL impurity pellet injection[41]. As an example, figure 12 shows time traces of the $B_V 495nm$ active charge exchange intensity during a LBO boron-carbide injection. The ability of the CXRS to provide absolute density profiles of the fully stripped ion at time resolutions down to a few milliseconds during these injection events makes the combination an extremely powerful tool for the investigation of impurity transport in W7-X.

E. Argon density for XICS Calibration

As well as line integrated measurements of T_i and E_r, the X-ray spectrometer measures the density of the observed ionisation states of argon. XICS measurements were conducted in almost all shots of the previous campaigns, using a trace argon injection equivalent to $10^{-5}n_e$. While extremely useful for dynamic transport studies[42], an absolute calibration has not been carried out so far. In order to open the possibility of cross-calibrating the XICS, two argon emission lines that result from charge exchange to ions observed by the XICS were investigated. The first of these, Ar_{XVIII} at $344.9nm$ was not observable due to low optical transmission of the CXRS system in the near-UV. However, the Ar_{XVI} line at $436.5nm$ produced a good signal. Figure 11 shows the derived normalised concentration profiles (derived as in section IV D) compared to those determined from the XICS[38]. Agreement in the concentration profile shape can be seen despite the neglect of the charge exchange

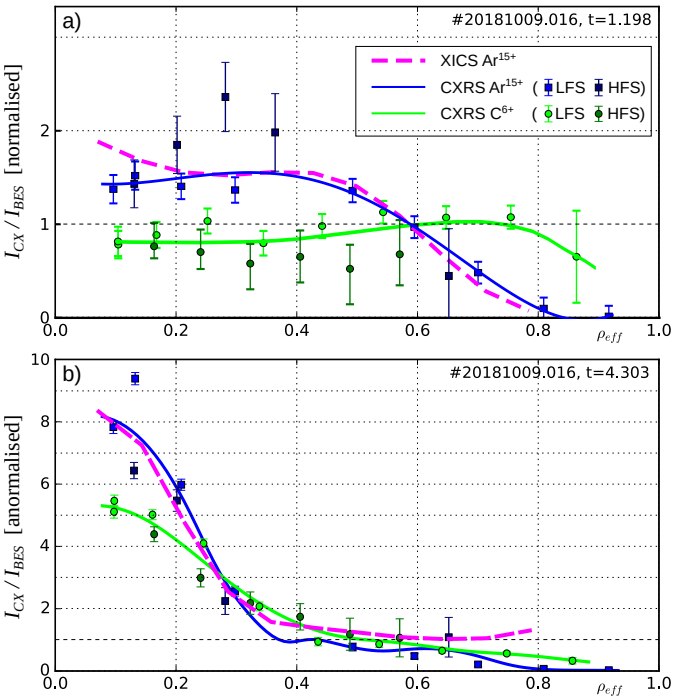

FIG. 11. Approximate profile shape of argon (blue) and carbon (green) densities derived by ratio of charge exchange intensity to full energy beam emission intensity at a) the start and b) the end of a purely NBI heated discharge. Normalised argon density profiles derived from a Bayesian inversion of XICS intensities[38] are shown in magenta. All three quantities are normalised to their values at $\rho = 0.6$ in a) and the same factors used for b).

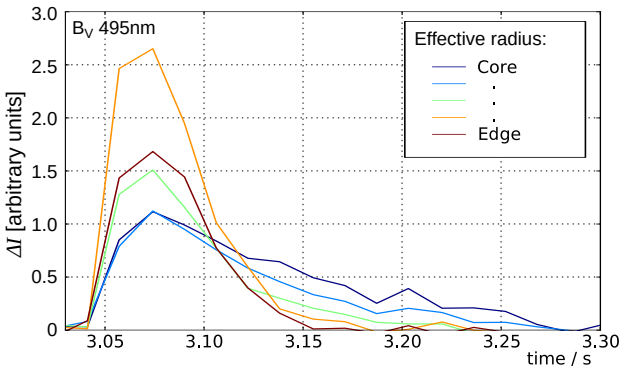

FIG. 12. Time traces of active charge exchange intensity from the $B_V 495nm$ line during boron-carbide injection by the W7-X Laser blow-off system.

emission coefficients and their dependence on the plasma parameters, most likely due to lack of variation of those parameters over the profile in figure 11a and due to the dominance of the impurity peaking feature in 11b. Correction for the halo contribution is likely to reduce the peaking in the core to some extent, but it is clear that the peaking will still be present in the argon concentration as well as the carbon. If absolute densities can be determined for these shots from CXRS, it would be possible to determine the XICS sensitivity which would allow absolute argon concentrations to be derived for shots with no neutral injection, which is the majority from the last campaign. The calculation will depend on the availability of accurate charge exchange cross-sections for these argon lines which is currently of some concern, since existing cross-section data sets vary significantly. This data is presently being experimentally investigated at other machines, an effort which the W7-X combination of CXRS and XICS will be able to assist.

F. High resolution temperature profiles

While the variable wavelength spectrometers allow the flexibility to measure two other impurities simultaneously to the carbon from the ILS, the C^{VI} line has by far the strongest intensity. Since the three spectrometers use interleaved lines of sight, the highest resolution and highest signal-to-noise profiles are achieved by selecting the C^{VI} on both variable wavelength spectrometers. Figure 13a shows the profile quality that can be achieved for a single time slice. Reasonable consistency is achieved between the different spectrometers with agreement within the statistical uncertainty shown. Only within $\rho_{\text{eff}} < 0.2$ do the toroidal lines of sight give a slightly elevated temperature than the other measurements. This is most likely due to the effect of the line-integration across the width of the beam, which is neglected in this analysis, and leads to a slight disagreement between the different viewing geometries, particularly the **T** port system, which averages over a relatively large range of radii (see figure 3).

Probably the most important use of T_i profiles is for the determination of gradients used in the calculation of heat transport and in the assesment of turbulence mechanisms. Since gradients are extremely sensitive to even small statistical and systematic errors in the measurements, data with the demonstrated high resolution can be critically important[43]. Figure 13a includes a moving regression based on Nadaraya-Watson kernel estimation, using a fixed scale length of 3cm ($\Delta\rho_{\text{eff}} \sim 0.06$). This fitting method is chosen as an example, as it is robust and avoids spurious osciallations. Figure 13b shows the derived temperature gradient and the error bands shown are the result of fits to each individual spectrometer and optical system with identical fitting parameters as for the combined data. These result in quite a large variation of possible gradients and show clearly that high resolution and signal to noise are required to determine even reasonable gradient profiles. The diversity of spectrometers and viewing angles in the W7-X CXRS system help to mitigate the effect of systematic errors in any one of the systems due to e.g. alignment errors, passive background or line of sight integration effects.

G. Summary and future work

A highly flexible charge exchange recombination spectroscopy system has been designed, installed and suc-

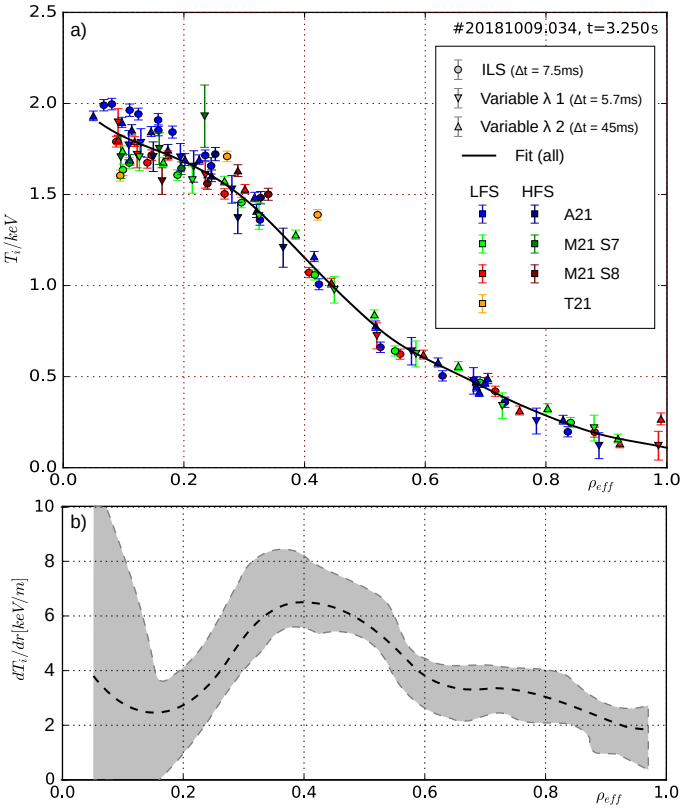

FIG. 13. a) High resolution carbon temperature profiles from combination of all spectrometers (symbols) and all observation systems (colors) and a kernel regression fit (black) with scale length of $\Delta\rho_{\text{eff}} \sim 0.06$. b) Derived temperature gradient from fit to all data points. Systematic error band shown from min/max of fits to each individual spectrometer/observation system.

cessfully operated during the 2018 campaign of the optimised stellarator W7-X. The design was focused on the delivery of high quality, high resolution primary measurements (T_i, E_r and n_Z) despite electron densities up to $2 \times 10^{19} m^{-3}$ and small flows of less than $10 km/s$.

Ion temperature profiles of sufficient quality for detailed ion heat flux analysis have been derived and first steps towards good quality profiles of radial electric field, toroidal velocity, impurity densities and beam deposition have been made, with good data quality under typical conditions. Some difficulty in separation of active and passive charge exchange signals during long pulses has been identified and will be a strong focus of future work. Together with the H_α spectrum, this is a strong candidate to benefit from forward modelling and Bayesian analysis, whereby a single consistent forward model of the neutral beam and impurity flows would be fitted to the raw spectral data from all channels of all spectrometers simultaneously, including the passive spectrometer that does not observe the heating beam. This would allow a single self-consistent determination of all the plasma parameters mentioned here, and due to the resulting more favourable data point to free-parameter ratio, is expected to strongly alleviate the problems of the passive emission and the complexity of the beam spectra.

H. Acknowledgements

The authors would like to thank Eindhoven University, Forschungszentrum Jülich and the Netherlands Organisation for applied scientific research (TNO) for the loan of the ITER-like spectrometer. This work has been carried out within the framework of the EUROfusion Consortium and has received funding from the Euratom research and training programme 2014-2018 and 2019-2020 under grant agreement No 633053. The views and opinions expressed herein do not necessarily reflect those of the European Commission.

[1] T. Pedersen *et al.*, "Key results from the first plasma operation phase and outlook for future performance in wendelstein 7-x," Physics of Plasmas **24**, 055503 (2017), https://doi.org/10.1063/1.4983629.

[2] R. Wolf *et al.*, "Major results from the first plasma campaign of the wendelstein 7-x stellarator," Nuclear Fusion **57**, 102020 (2017).

[3] T. Klinger *et al.*, "Overview of first wendelstein 7-x high-performance operation," Nuclear Fusion (2019).

[4] N. A. Pablant *et al.*, "Core radial electric field and transport in wendelstein 7-x plasmas," Physics of Plasmas **25**, 022508 (2018), https://doi.org/10.1063/1.4999842.

[5] E. Pasch *et al.*, "The Thomson scattering system at Wendelstein 7-X," Review of Scientific Instruments **87**, 11E729 (2016), http://aip.scitation.org/doi/pdf/10.1063/1.4962248.

[6] Hirsch, Matthias *et al.*, "Ece diagnostic for the initial operation of wendelstein 7-x," EPJ Web Conf. **203**, 03007 (2019).

[7] J. Knauer *et al.*, "A new dispersion interferometer for the stellarator wendelstein 7-x," in *Proc. of the 43rd EPS Conf. on Plasma Physics, Leuven, Belgium*, P4.017 (2016).

[8] A. Langenberg *et al.*, "Prospects of x-ray imaging spectrometers for impurity transport: Recent results from the stellarator wendelstein 7-x," Review of Scientific Instruments **89**, 10G101 (2018), https://doi.org/10.1063/1.5036536.

[9] N. A. Pablant *et al.*, "Tomographic inversion techniques incorporating physical constraints for line integrated spectroscopy in stellarators and tokamaks," Review of Scientific Instruments **85**, 11E424 (2014).

[10] A. Pavone *et al.*, "Measurement and automatic bayesian inference of the effective plasma charge zeff from visible bremsstrahlung in w7-x." in *Proc. of the 3rd European Conference on Plasma Diagnostics, Lisbon, Portugal* (2019).

[11] P. McNeely *et al.*, "Commissioning and initial operation of the w7-x neutral beam injection heating system (submitted)," Fusion Engineering and Design (2019), 14th International Symposium on Fusion Nuclear Technology.

[12] R. J. Fonck *et al.*, "Determination of plasma-ion velocity distribution via charge-exchange recombination spectroscopy," Phys. Rev. A **29**, 3288–3309 (1984).

[13] R. C. Isler, "An overview of charge-exchange spectroscopy as a plasma diagnostic," Plasma Physics and Controlled Fusion **36**, 171–208 (1994).

[14] K. Ida *et al.*, "Measurements of poloidal rotation velocity using charge exchange spectroscopy in a large helical device," Review of Scientific Instruments **71**, 2360–2366 (2000), https://doi.org/10.1063/1.1150621.

[15] R. McDermott *et al.*, "Extensions to the charge exchange recombination spectroscopy diagnostic suite at asdex upgrade," Review of Scientific Instruments **88**, 073508 (2017), https://doi.org/10.1063/1.4993131.

[16]W. Mandl *et al.*, "Beam emission spectroscopy as a comprehensive plasma diagnostic tool," Plasma Physics and Controlled Fusion **35**, 1373–1394 (1993).

[17]R. C. Wolf *et al.*, "Electron-cyclotron-resonance heating in wendelstein 7-x: A versatile heating and current-drive method and a tool for in-depth physics studies," Plasma Physics and Controlled Fusion **61**, 014037 (2018).

[18]E. Viezzer *et al.*, "High-resolution charge exchange measurements at asdex upgrade," Review of Scientific Instruments **83**, 103501 (2012), https://doi.org/10.1063/1.4755810.

[19]R. König *et al.*, "Diagnostics design for steady-state operation of the wendelstein 7-x stellarator," Review of Scientific Instruments **81**, 10E133 (2010), https://doi.org/10.1063/1.3483210.

[20]R. J. E. Jaspers *et al.*, "A high etendue spectrometer suitable for core charge exchange recombination spectroscopy on iter," Review of Scientific Instruments **83**, 10D515 (2012), https://doi.org/10.1063/1.4732058.

[21]A. Kappatou *et al.*, "Method to obtain absolute impurity density profiles combining charge exchange and beam emission spectroscopy without absolute intensity calibration," Review of Scientific Instruments **83**, 10D519 (2012), https://doi.org/10.1063/1.4732847.

[22]A. Kappatou *et al.*, "A forward model for the helium plume effect and the interpretation of helium charge exchange measurements at ASDEX upgrade," Plasma Physics and Controlled Fusion **60**, 055006 (2018).

[23]A. Blom and C. Jup$eacute$n, "Parametrization of the zeeman effect for hydrogen-like spectra in high-temperature plasmas," Plasma Physics and Controlled Fusion **44**, 1229–1241 (2002).

[24]M. von Hellermann *et al.*, "Analytical approximation of cross-section effects on charge exchange spectra observed in hot fusion plasmas," Plasma Physics and Controlled Fusion **37**, 71–94 (1995).

[25]S. Bozhenkov *et al.*, "The thomson scattering diagnostic at wendelstein 7-x and its performance in the first operation phase," Journal of Instrumentation **12**, P10004 (2017).

[26]W. M. Solomon *et al.*, "Extraction of poloidal velocity from charge exchange recombination spectroscopy measurements," Review of Scientific Instruments **75**, 3481–3486 (2004), https://doi.org/10.1063/1.1790042.

[27]J. Arévalo *et al.*, "Incompressibility of impurity flows in low density TJ-II plasmas and comparison with neoclassical theory," Nuclear Fusion **53**, 023003 (2013).

[28]A. Alonso *et al.*, "Understanding ion and impurity flows in the wendelstein 7-x stellarator," in *Proc. of the 46th EPS Conference on Plasma Physics, Milan, Italy*, I3.102 (2019).

[29]H. Sugama and S. Nishimura, "How to calculate the neoclassical viscosity, diffusion, and current coefficients in general toroidal plasmas," Physics of Plasmas **9**, 4637–4653 (2002), https://doi.org/10.1063/1.1512917.

[30]W. I. van Rij and S. P. Hirshman, "Variational bounds for transport coefficients in three-dimensional toroidal plasmas," Physics of Fluids B: Plasma Physics **1**, 563–569 (1989), https://doi.org/10.1063/1.859116.

[31]M. Salewski *et al.*, "Deuterium temperature, drift velocity, and density measurements in non-maxwellian plasmas at ASDEX upgrade," Nuclear Fusion **58**, 036017 (2018).

[32]E. Delabie *et al.*, "Consistency of atomic data for the interpretation of beam emission spectra," Plasma Physics and Controlled Fusion **52**, 125008 (2010).

[33]M. De Bock *et al.*, "Measuring one-dimensional and two-dimensional impurity density profiles on textor using combined charge exchange-beam emission spectroscopy and ultrasoft x-ray tomography," Review of Scientific Instruments **75**, 4155–4157 (2004), https://doi.org/10.1063/1.1787600.

[34]R.M.McDermott *et al.*, "Evaluation of impurity densities from charge exchange recombination spectroscopy measurements at ASDEX upgrade," Plasma Physics and Controlled Fusion **60**, 095007 (2018).

[35]L. Vano *et al.*, "Studies on carbon content and transport with charge exchange spectroscopy on w7-x," in *Proc. of the 46th EPS Conference on Plasma Physics, Milan, Italy*, P5.1065 (2019).

[36]R.Brakel *et al.*, "Strategy and optimisation of wall conditioning at the wendelstein 7-x stellarator," in *Proc. 27th IAEA Fusion Energy Conf, India* (2018) pp. EX/P8–17.

[37]R. Burhenn *et al.*, "On impurity handling in high performance stellarator/heliotron plasmas," Nuclear Fusion **49**, 065005 (2009).

[38]A. Langenberg *et al.*, "Inference of temperature and density profiles via forward modeling of an x-ray imaging crystal spectrometer within the minerva bayesian analysis framework," Review of Scientific Instruments **90**, 063505 (2019), https://doi.org/10.1063/1.5086283.

[39]T. Wegner *et al.*, "Design, capabilities, and first results of the new laser blow-off system on wendelstein 7-x," Review of Scientific Instruments **89**, 073505 (2018), https://doi.org/10.1063/1.5037543.

[40]A. Nagy *et al.*, "A horizontal powder injector for W7-X," Fusion Engineering and Design **146**, 1403–1407 (2019).

[41]R. Bussiahn *et al.*, "Tracer-encapsulated solid pellet (tespel) injection system for wendelstein 7-x," Review of Scientific Instruments **89**, 10K112 (2018), https://doi.org/10.1063/1.5038844.

[42]A. Langenberg *et al.*, "Argon impurity transport studies at wendelstein 7-x using x-ray imaging spectrometer measurements," Nuclear Fusion **57**, 086013 (2017).

[43]S. Bozhenkov *et al.*, "High-performance pellet experiments in wendelstein 7-x." Nuclear Fusion ((submitted Nov. 2019)).